

Evidence For Cloud-Cloud Collision and Parsec-Scale Stellar Feedback Within the L1641-N Region

Fumitaka Nakamura^{1,2}, Tomoya Miura³, Yoshimi Kitamura², Yoshito Shimajiri⁴, Ryohei Kawabe⁴, Norio Ikeda², Takashi Tsukagoshi⁵, Munetake Momose⁶, Ryoichi Nishi³, and Zhi-Yun Li⁷

Received _____; accepted _____

¹National Astronomical Observatory, Mitaka, Tokyo 181-8588, Japan; fumi-taka.nakamura@nao.ac.jp

²Institute of Space and Astronautical Science, Japan Aerospace Exploration Agency, 3-1-1 Yoshinodai, Sagamihara, Kanagawa 229-8510, Japan

³Department of Physics, Niigata University, 8050 Ikarashi-2, Niigata, 950-2181, Japan

⁴Nobeyama Radio Observatory, Minamimaki, Minamisaku, Nagano 384-1805, Japan

⁵Institute of Astronomy, Faculty of Science, University of Tokyo, Osawa 2-21-1, Mitaka, Tokyo, 181-0015, Japan

⁶Institute of Astrophysics and Planetary Sciences, Ibaraki University, Bunkyo 2-1-1, Mito 310-8512, Japan

⁷Department of Astronomy, University of Virginia, P. O. Box 400325, Charlottesville, VA 22904; zl4h@virginia.edu

ABSTRACT

We present high spatial resolution ^{12}CO ($J = 1 - 0$) images taken by the Nobeyama 45m telescope toward a $48' \times 48'$ area including the L1641-N cluster. The effective spatial resolution of the maps is $21''$, corresponding to 0.04 pc at a distance of 400 pc. A recent 1.1 mm dust continuum map reveals that the dense gas is concentrated in several thin filaments. We find that a few dust filaments are located at the parts where ^{12}CO ($J = 1 - 0$) emission drops sharply. Furthermore, the filaments have two-components with different velocities. The velocity difference between the two-components is about 3 km s^{-1} , corresponding to a Mach number of 10, significantly larger than the local turbulent velocity in the cloud. These facts imply that the collision of the two components (hereafter, the cloud-cloud collision) possibly contributed to the formation of these filaments. Since the two components appear to overlap toward the filaments on the plane of the sky, the collision may have occurred almost along the line of sight. Star formation in the L1641-N cluster was probably triggered by such a collision. We also find several parsec-scale CO shells whose centers are close to either the L1641-N cluster or V 380 Ori cluster. We propose that these shells were created by multiple winds and/or outflows from cluster YSOs, i.e., “protocluster winds.” One exceptional dust filament located at the western cloud edge lies along a shell; it is presumably a part of the expanding shell. Both the cloud-cloud collision and protocluster winds are likely to influence the cloud structure and kinematics in this region.

Subject headings: ISM:structure — ISM: clouds — ISM: kinematics and dynamics — stars: formation

1. Introduction

Most stars form in giant molecular clouds (GMCs). In GMCs, various environmental effects such as large-scale flows, supernovae, and stellar feedback from young stars (winds, radiation, and outflows) often shape the cloud structure and dynamics, triggering and suppressing the formation of the next-generation stars (e.g., McKee & Ostriker 2007). Recent numerical simulations of star formation have demonstrated that these effects significantly influence, or even control, the cloud evolution and star formation (Mac Low & Klessen 2004; Krumholz et al. 2011; Li & Nakamura 2006; Nakamura & Li 2007; Banerjee et al. 2009; Carroll et al. 2009; Gritschneider et al. 2009; Vazquez-Semadeni et al. 2010). Fingerprints of these environmental effects have been found in some star-forming regions (e.g., Bally 1989; Heyer et al. 1992; Bally 2008; O’Dell et al. 2008; Sandell & Knee 2001; Shimajiri et al. 2008; Arce et al. 2010; Shimajiri et al. 2011). However, the roles of the environmental effects in star formation remain poorly understood observationally. This is partly because wide-field, high spatial and/or spectral resolution observations, which are needed to resolve the cloud structure and kinematics in detail, are still limited. In particular, stellar feedbacks such as winds or outflows are often extended to parsec-scale (e.g., Heyer et al. 1992). Wide-field observations of the cloud structure and kinematics are needed to unveil such environmental effects. At the same time, it is necessary to resolve the cloud structure at a scale of “dense cores”, which are the basic units of individual star formation (≈ 0.1 pc \sim one arcmin at a distance of 400 pc), in order to uncover a link between individual star formation and the environmental effects.

In this paper, to understand how the environmental effects influence the internal structure and kinematics in star-forming molecular clouds, we present the results of wide-field ^{12}CO ($J = 1 - 0$) mapping observations toward the L1641-N region, a nearby active star-forming region in the Orion A giant molecular cloud complex, using the

Nobeyama 45 m radio telescope. Our data have high angular ($\approx 21''$) resolution, allowing us to resolve spatial structures at a scale of 0.04 pc at a distance of 400 pc (see e.g., Menten et al. 2007; Sandstrom et al. 2007; Hirota et al. 1992). By comparing the ^{12}CO ($J = 1 - 0$) map with the 1.1 mm dust continuum map taken by the AzTEC camera on the ASTE telescope, we investigate how the dense gas is distributed in the parent molecular cloud.

The L1641-N region is one of the well-studied, nearby star-forming regions (Allen & Davis 2008, and references therein). It lies just south the clouds known as OMC-4 and OMC-5, making up a northern part of the L1641 molecular cloud, one of the several $\sim 10^4 M_\odot$ molecular clouds contained within the Orion A giant molecular cloud complex. The L1641 cloud is a filamentary cloud extending more than $2 - 3$ degrees ($15 \sim 20$ pc) and having numerous clumpy elongated condensations with typical masses of a few tens to $\sim 10^2 M_\odot$ and sizes of a few tenths to ~ 1 pc. This cloud is not forming massive stars: its most massive member is the B4 V Herbig Ae/Be star, HD 38023, at the position of (R.A., Dec.) = (5:42:21, $-8:08$), located at the L1641-S region. Although it has no rich clusters comparable to the Orion Nebula Cluster, the L1641-N region consists of several active star-forming regions. Optical, X-ray, and infrared surveys have revealed that most of the protostars are clustered in small clusters or groups with a few $\times 10$ YSOs (Strom et al. 1993; Carpenter et al. 2001). A prominent example is the L1641-N cluster which contains approximately 80 YSOs (Galfalk & Olofsson 2008; Fang et al. 2009), having the stellar surface density of $\sim 200 \text{ pc}^{-2}$, an order of magnitude larger than the average stellar surface density of the distributed population of YSOs. The most luminous object in this cluster is IRAS 05338-0624, around which powerful molecular outflows were discovered (Fukui et al. 1986; Stanke & Williams 2007).

Another example is the V 380 Ori cluster. V 380 Ori itself is a binary of Herbig Ae/Be

stars, illuminating the reflection nebula NGC1999 (Baines et al. 2006). Many Harbig-Haro (H-H) objects were discovered in this region (Allen & Davis 2008, and references therein). The most famous and spectacular outflows are H-H 1/2, which are associated with gigantic bow shocks. Heyer et al. (1992) discovered a parsec-scale expanding shell around the V 380 Ori star from the ^{13}CO ($J = 1 - 0$) observations, suggesting that star formation activity indeed shapes cloud structure and dynamics significantly. These two clusters do not contain massive stars that would emit strong UV radiation and control the evolution of the region. The L1641-N region is expected to provide us with clues to understanding the impact of the current and previous star formation activity on the cloud structure and kinematics.

The rest of the paper is organized as follows. The details of our observations and data are described in Sections 2 and 3. We present results of our ^{12}CO ($J = 1 - 0$) observations in Section 4, and discuss the cloud structure and star formation activity of this region in Section 5. Finally, we summarize our conclusion in Section 6.

2. Observations

The ^{12}CO ($J = 1 - 0$; 115.271204 GHz) observations were carried out with the 25-element focal plane receiver BEARS on the Nobeyama Radio Observatory (NRO) 45 m telescope. They cover a $48' \times 48'$ area including the L1641-N cluster, the northern part of the L1641 molecular cloud, from 2009 December to 2010 January. At 115 GHz, the telescope has a FWHM beam size of $15''$ and a main beam efficiency, η , of 0.32. At the back end, we used 25 sets of 1024 channel auto-correlators (ACs) which have bandwidths of 32 MHz and frequency resolutions of 37.8 kHz. The frequency resolution corresponds to a velocity resolution of 0.1 km s^{-1} at 115 GHz. During the observations, the system noise temperatures were in the range between 300 to 600 K in DSB at the observed elevations. The standard chopper wheel method was used to convert the output signal into the antenna

temperatures (T_{A}^*), corrected for the atmospheric attenuation. Our mapping observations were made by the On-The-Fly (OTF) mapping technique. We adopted a spheroidal function as a gridding convolution function (GCF) to calculate the intensity at each grid point of the final cube data with a spatial grid size of $7.5''$ and a velocity resolution of 0.5 km s^{-1} . The final effective resolution of the map is $21''$, corresponding to 0.04 pc at the distance to Orion A of 400 pc . The rms noise level of the final map is 0.39 K in T_{A}^* .

3. Other Data

In the next section, we compare our ^{12}CO ($J = 1 - 0$) data with 1.1 mm continuum, ^{13}CO ($J = 1 - 0$), and H^{13}CO^+ ($J = 1 - 0$) data. Here, we briefly describe these data.

The 1.1 mm continuum data were taken toward a $1.7^\circ \times 2.3^\circ$ region in the northern part of the Orion A giant molecular cloud complex with the AzTEC camera mounted on the ASTE 10 m telescope (Shimajiri et al. 2011). The observations were carried out in the period from October to December 2008. The noise level was about 9 mJy beam^{-1} and the effective beam size was $40''$, about twice that of the ^{12}CO map, after the FRUIT imaging which is an iterative mapping method to recover the spatially-extended component. The detail of the data is given in Shimajiri et al. (2011).

The ^{13}CO ($J = 1 - 0$) data were taken by Bally & Langer (1987) with the 7 m telescope of the AT&T Bell Laboratories. The original data covers the whole Orion A giant molecular cloud complex (see Bally & Langer 1987; Bally 1989), much larger area than that of our ^{12}CO ($J = 1 - 0$) data. The observations were carried out in the period from 1984 to 1986. The grid size of the data was $60''$, about three times coarser than that of our ^{12}CO ($J = 1 - 0$) data. The rms noise level was about 0.3 K in T_{A}^* at the velocity resolution of about 0.27 km s^{-1} . The main beam efficiency of the 7 m telescope was 0.9 .

The H^{13}CO^+ ($J = 1 - 0$) data were taken from the Nobeyama 45 m archival data. The data were obtained from December 1999 to April 2004 in the position-switching mode, with a grid size of $21''$. The rms noise level was 0.1 K in T_{A}^* at the velocity resolution of about 0.13 km s^{-1} with a main-beam efficiency of 0.51. See <http://www.nro.nao.ac.jp/> for more detail.

4. Results

4.1. Global ^{12}CO ($J = 1 - 0$) and ^{13}CO ($J = 1 - 0$) Distributions

In Figure 1, we present a ^{12}CO ($J = 1 - 0$) total integrated intensity map toward the $48' \times 48'$ area including the L1641-N cluster. The ^{12}CO ($J = 1 - 0$) emission tends to be optically thick in the entire molecular cloud, thus representing the spatial extent of the global molecular gas distribution, instead of the density distribution. For comparison, in Figure 1(b), the 1.1 mm continuum map taken by the AzTEC camera mounted on the ASTE 10 m telescope is overlaid on the ^{12}CO ($J = 1 - 0$) total integrated intensity map with the contours.

The ^{12}CO ($J = 1 - 0$) integrated intensity map indicates that the parent filamentary cloud is roughly running from north to south. The filament appears to bifurcate in the southern part of the image. At the bifurcation point, the L1641-N cluster resides. The most intense ^{12}CO emission is associated with the L1641-N cluster at the position of (R.A., Dec.) = (5:36:18, $-6:21:48$). The position of the ^{12}CO integrated intensity peak almost coincides with that of the bright, compact continuum source, L1641-N MM1 identified by Stanke & Williams (2007) with the SMA interferometer, although it deviates about $22''$ toward south. This is probably because the single-dish continuum peak traces the whole clumpy structures identified by SMA, including L1641-N MM1, as shown in Figure 6 of

Stanke & Williams (2007). Comparison between the 1.1 mm continuum image and the ^{12}CO integrated intensity map indicates that several filamentary dense clumps are located near the parts where the ^{12}CO emission drops sharply. These parts are in good agreement with the edges traced by ^{13}CO ($J = 1 - 0$) emission (see Fig. 2) and therefore, hereafter, we refer to these parts as the cloud edges, for simplicity. For comparison, several main filamentary dense clumps are labeled with alphabet A through E in Figure 1(b), indicating that the filaments A and E are located at the eastern and western cloud edges, respectively.

In Figure 2, we also present the ^{13}CO ($J = 1 - 0$) integrated intensity map toward the same area shown in Figure 1. Since the fractional abundance of ^{13}CO is smaller than that of ^{12}CO by a factor of about 40, the ^{13}CO emission tends to be optically thinner than the ^{12}CO emission, and thus its spatial distribution is expected to represent the distribution of molecular gas with intermediate densities of about 10^3 cm^{-3} . Although the spatial extent of the ^{13}CO integrated intensity is well covered by that of ^{12}CO , its spatial distribution appears different from that of ^{12}CO . The ^{13}CO emission tends to be concentrated in elongated or filamentary structures, which reasonably trace the parsec-scale filamentary clumps identified by the 1.1 mm dust continuum emission (see Figure 2). The 1.1 mm dust continuum emission and ^{13}CO ($J = 1 - 0$) integrated intensity also take their maxima nearly at the same position, i.e., toward the L1641-N cluster center, suggesting that the dense gas is concentrated into the L1641-N cluster-forming filamentary clump (the filament C).

In Figure 3, we present a ^{12}CO ($J = 1 - 0$) peak intensity map, which indicates that the ^{12}CO ($J = 1 - 0$) emission drops sharply both at the eastern and western sides of the parent filamentary cloud. At the same places, the ^{12}CO and ^{13}CO integrated intensity drops sharply. A prominent feature is the existence of many arcs or elongated structures, most of which tend to be across the filamentary structures traced by the ^{13}CO ($J = 1 - 0$)

integrated intensity map. The peak intensity map of the optical thick ^{12}CO ($J = 1 - 0$) emission typically represents the distribution of the excitation temperature, instead of the local density distribution. However, the structures traced by the ^{12}CO ($J = 1 - 0$) peak intensity map are sometimes seen in the ^{13}CO ($J = 1 - 0$) integrated intensity map and is therefore likely to reflect the cloud density distribution in some parts. For example, some arcs located at the southwest part near the cloud edge are recognized in both the ^{12}CO ($J = 1 - 0$) peak intensity and ^{13}CO integrated intensity maps (e.g., (R.A., Dec.) \simeq (5:35:0, –6:40:0) and (5:35:30, –6:35:30)).

4.2. Dust Filaments

Here, we present several aspects of the parsec-scale filamentary dust clumps, by comparing the spatial distributions of several molecular emission lines such as ^{12}CO ($J = 1 - 0$) and ^{13}CO ($J = 1 - 0$) with the 1.1 mm continuum emission.

The dust filaments are likely to have high densities $\sim 10^{4-5} \text{ cm}^{-3}$ because the CS ($J = 1 - 0$) emission is detected toward all the dust filaments (see Figure 5(c) of Tatematsu et al. 1993). The H^{13}CO^+ ($J = 1 - 0$) emission is also detected toward the dense parts of the filaments (Ikeda et al. 2007). For comparison, we show in Figure 4 the H^{13}CO^+ ($J = 1 - 0$) integrated intensity contours overlaid on the 1.1 mm image, in which the dust filaments are labeled with A through E. Figure 4 indicates that the strongest H^{13}CO^+ ($J = 1 - 0$) emission comes from the most massive filament C associated with the L1641-N cluster. The H^{13}CO^+ emission peaks in this filament coincide reasonably well with those of the 1.1 mm continuum emission. The line-of-sight velocities of the H^{13}CO^+ ($J = 1 - 0$) peaks are around 7 km s^{-1} . Interestingly, the CS ($J = 1 - 0$) emission is strongest at $V_{\text{LSR}} \sim 10 \text{ km s}^{-1}$, but weaker at $V_{\text{LSR}} \sim 7 \text{ km s}^{-1}$ (see Figure 5(c) of Tatematsu et al. 1993), although the H^{13}CO^+ emission is strong at around 7 km s^{-1} . In addition, the CS emission

associated with the massive filament C is distributed in the wide velocity range of 6 km s⁻¹ to 12 km s⁻¹. As mentioned below, the CS emission as well as ¹²CO indicates that the most massive filament C has two different velocity components, which may give us a clue to understand the formation mechanism of the filament. We note that the filament A is out of the area observed by Ikeda et al. (2007), but it is detected in CS ($J = 1 - 0$) obtained by Tatematsu et al. (1993). Thus, the filament contains the dense gas with densities of 10⁴⁻⁵ cm⁻³.

The ¹²CO ($J = 1 - 0$) velocity channel maps presented in Figure 5 indicate that the velocity structure in this region can be divided into three components: blueshifted (3–6 km s⁻¹), main (7–9 km s⁻¹), and redshifted ones (10–14 km s⁻¹). For comparison, we present in Figure 6 a two-color image with redshifted ¹²CO integrated intensity in red and blueshifted ¹²CO integrated intensity in blue. The 1.1 mm continuum map is overlaid on the image with white contours. The integration ranges are 9.5 ~ 14.5 km s⁻¹ and 3.5 ~ 6.5 km s⁻¹ for the redshifted and blueshifted components, respectively. The two-color image indicates that the redshifted component is dominant in the upper half of the parent filament, whereas the blueshifted component is dominant in the lower half.

The strong blueshifted component with a velocity range between 4 and 6 km s⁻¹ appears in the southern part where the filament C and the L1641-N cluster reside. The redshifted component with a velocity of 10 to 12 km s⁻¹ is also associated with the massive filament C. The presence of a couple of velocity components toward the filament C is more clearly seen in the position-velocity map presented in Figure 7(c), showing that the filament consists of two separate components with different velocities toward the eastern part of the filament: one is about 6 km s⁻¹ and the other is 9 km s⁻¹. These two-components with different velocities are in good agreement with the CS map by Tatematsu et al. (1993). The filament is surrounded by the blueshifted elongated component that apparently have

a head-tail shape (see also Figure 6). Another faint velocity component is seen toward the western part of the filament at the velocity of about 11 km s^{-1} . This component is more evident in the position-velocity diagrams of the ^{13}CO ($J = 1 - 0$) emission (see Figure 8(c)).

Other dust filaments also have two-component velocity structures. The position-velocity diagram (Figure 7(b)) indicates that the filament A, located at the eastern cloud edge, has two-components with different velocities: a diffuse component is at 6 km s^{-1} and stronger emission component is at 9 km s^{-1} . The similar velocity components are associated with the filaments B and D (see also Figure 5). The two-color image indicates that the eastern area outside the parent cloud is filled with the diffuse component with about 6 km s^{-1} . According to Sakamoto et al. (1997) and Shimajiri et al. (2011), this diffuse component is distributed in the much larger area in the eastern area of the Orion A giant molecular cloud complex. The filament E has the two-components at 7 km s^{-1} and 9.5 km s^{-1} (see Figure 7(e)). These velocity structures of the filaments are in good agreement with the position-velocity map of the ^{13}CO ($J = 1 - 0$) emission (see Figure 8(e)). It is worth noting that the two filaments labeled with A and E are located near the cloud edges where the ^{12}CO ($J = 1 - 0$) emission drops sharply.

4.3. Shells

Besides the filamentary structures, shell-like structures are prominent in our ^{12}CO map, particularly in the peak intensity map. In this subsection, we describe some characteristics of these shell-like structures in detail.

In the ^{12}CO ($J = 1 - 0$) integrated intensity map (Figure 1), a shell-like structure can be recognized at the position of (R.A., Dec.) $\sim (5:36:9, -6:4:20)$. The radius of the shell is about $10'$, corresponding to about 1 pc at a distance of 400 pc . The shell is more clearly

seen in the ^{13}CO ($J = 1 - 0$) integrated intensity map presented in Figure 2. This shell was first found by Heyer et al. (1992) who carried out a wide-field mapping observation in ^{13}CO ($J = 1 - 0$) toward the Orion A giant molecular cloud complex with the FCRAO 14 m telescope. They found that the shell has two velocity components with a velocity difference of about $2\text{--}3 \text{ km s}^{-1}$, implying that it has an expanding motion. They also found a number of large holes surrounded by expanding shells. The typical radius of the shells is $10' - 26'$, corresponding to $1\text{--}3 \text{ pc}$ at a distance of 400 pc . They interpreted that these structures stem from events associated with the energetic star formation activity within the cloud.

Similar shell-like structures can be seen in our ^{12}CO maps. For example, in the central part of the ^{12}CO peak intensity map, two prominent thin shell structures are seen (Figure 3). We labeled these shells by A1 and A2 on the peak intensity map presented in Figure 9. There is also a shell labeled by A3, which is almost parallel to the A1 and A2 shells. These three shells are spatially well-ordered and appear to have a common center which is very close to the position of the L1641-N cluster. These shells have very small thickness of about $30''$. Such a thin shell may be difficult to be found in the ^{13}CO map because of the spatial resolution.

Another prominent shell-like structure can be recognized in the southern part of the CO integrated intensity maps (Figures 1 and 2), where the CO emission appears weak. Here, we labeled three remarkable shell-like structures or arcs by B1, B2, and B3, although there are several similar arcs seen in the image (Figure 9). These arcs appear to be spatially well-ordered and homocentric. Some of them are detected in the CS ($J = 1 - 0$) line (see Figure 5(c) of Tatematsu et al. 1993), indicating that the dense gas is associated with them. We note that the common center of these shells is very close to the position of the V 380 Ori cluster, which is just outside our ^{12}CO map, located at (R.A., Dec.) = (5:36:25.43, $-6:42:57.7$).

The shells are also clearly seen in a volume rendering image of the ^{12}CO ($J = 1 - 0$) antenna temperature data presented in Figure 10. The volume rendering technique is suitable to find and visualize the coherent structures in the 3D space. The green color typically represents the areas with relatively high T_{A}^* of about 10–15 K. We designated the shells A1, A2, A3, B1, B2, and B3 in the image. These shells are coherent in the position-position-velocity cube, suggesting that they were created by some dynamical events. Several arcs, parts of the shells, can also be recognized in the ^{13}CO map presented in Figure 2. These coherent structures are remarkable since the surrounding gas is highly turbulent and such coherent structures would have been destroyed in a crossing time of the shells (about 10^4 yr for the radius of $10'' - 30''$ and velocity of 3 km s^{-1}). Their existence suggests that the events producing these coherent structures play a dominant role in determining the cloud internal structure. In Section 5.3 we will discuss these structures in detail.

4.4. Molecular Outflows in the L1641N cluster

Recent numerical simulations of cluster formation have suggested that protostellar outflow feedback plays an important role in regulating star formation in cluster-forming clumps because they inject substantial amount of kinetic energy into the surroundings (Li & Nakamura 2006; Nakamura & Li 2007; Carroll et al. 2009; Wang et al. 2010). Here, we attempt to identify molecular outflows associated with the L1641-N cluster to assess the roles of the outflow feedback in the dynamical evolution of the cloud. The ^{12}CO emission has been successfully adopted to identify high-velocity components driven by powerful protostellar outflows. (e.g., Stanke & Williams 2007; Takahashi et al. 2008; Arce et al. 2010; Nakamura et al. 2011a,b), and therefore we identify several molecular outflows in the L1641-N cluster using the ^{12}CO ($J = 1 - 0$) data.

Molecular outflow activity in the L1641-N region was first found by Fukui et al. (1986) at the position of the near-IR bright source IRAS 05338-0624 (see also Fukui et al. 1988). Further outflow surveys have been made through molecular line studies by several authors (e.g., Wilking et al. 1990; Stanke & Williams 2007). Stanke & Williams (2007) conducted ^{12}CO ($J = 2 - 1$) mapping observations toward the L1641-N cluster using the IRAM 30 m telescope and SMA interferometer, and identified a number of molecular outflow lobes. Recently, Davis et al. (2009) carried out a near-infrared H_2 survey of outflows in Orion A including the L1641-N region. To identify the molecular outflows, we first scrutinize the velocity channel maps of our ^{12}CO ($J = 1 - 0$) (Figure 5) and the position-velocity diagrams to find localized blueshifted and redshifted emission.

In Figure 11, we present the ^{12}CO ($J = 1 - 0$) integrated intensity contours overlaid on the 1.1 mm continuum image obtained by Shimajiri et al. (2011). The velocity intervals for the integration are $0 \sim 5 \text{ km s}^{-1}$ and $10 \sim 16 \text{ km s}^{-1}$ for blueshifted and redshifted components, respectively. Stanke & Williams (2007) labeled the outflow lobes identified from ^{12}CO ($J = 2 - 1$) whose names are also designated in Figure 11. The most extended collimated redshifted lobe identified by Stanke & Williams (2007), R-S, is not so prominent in our ^{12}CO ($J = 1 - 0$) map where this lobe is divided into several distinct knots. A number of H_2 knots labeled with SMZ 49 in Davis et al. (2009) are associated along this redshifted lobe. The blueshifted emission elongated along the northeast to southwest line is also seen north of the dust peak near the cluster center. This corresponds to the B-NE and B-N lobes in Stanke & Williams (2007). In the ^{12}CO ($J = 2 - 1$) map, this lobe has a Y shape, whereas in our ^{12}CO ($J = 1 - 0$) map, the B-NE emission dominates over the faint B-N emission. This ^{12}CO ($J = 1 - 0$) blueshifted lobe also corresponds to the one identified by Fukui et al. (1986). These are probably due to the fact that our ^{12}CO ($J = 1 - 0$) data tend to trace relatively low-velocity outflow components. In fact, according to Stanke & Williams (2007), at low velocities, the two lobes identified by the

^{12}CO ($J = 2 - 1$) emission blend together with a broad patch of ^{12}CO emission. The most intense dust continuum emission is associated with the area between the redshifted (R-S) and blueshifted (B-NE and B-N) lobes, which is in good agreement with the HCN and HCO^+ ridge found by Fukui et al. (1988) and the position of IRAS 05338-0624. The H_2 flows labeled with SMZ 51 and SMZ 53 appear to follow the B-NE and B-N lobes, respectively (see Fig. 6 of Davis et al. 2009).

Another highly-collimated, redshifted lobe is seen to the west of the R-S lobe, which is in good agreement with the R-SW lobe in Figure 2 of Stanke & Williams (2007). Similarly to the ^{12}CO ($J = 2 - 1$) map, this lobe appears not to have any obvious blueshifted counterlobe. The R-W, B-E, and B-SE2 lobes identified by Stanke & Williams (2007) can be clearly recognized in our map. The R-W lobe probably corresponds to the redshifted lobe identified by Fukui et al. (1986).

From our ^{12}CO map, the total outflow mass, momentum, and energy are estimated to about $13 M_\odot$, $80 M_\odot \text{ km s}^{-1}$, and $273 M_\odot \text{ km}^2 \text{ s}^{-2}$, respectively, by assuming the local thermodynamical equilibrium (LTE) condition and optically-thin emission. Here, we adopt the same systemic velocity of 7.5 km s^{-1} for all the outflow lobes and the values are corrected for the inclination angle $\xi = 57.3^\circ$ (Bontemps et al. 1996). The excitation temperature is adopted to 30 K, which is close to the peak brightness temperature of the ^{12}CO ($J = 1 - 0$) line profile at the L 1641-N cluster center. We also integrated the physical quantities in the velocity intervals of $0 \sim 5 \text{ km s}^{-1}$ and $10 \sim 16 \text{ km s}^{-1}$ for the blueshifted and redshifted components, respectively. We note that the physical quantities estimated above are insensitive to the assumed excitation temperature. The estimated quantities increase only by a few $\times 10\%$ over the range of $T_{\text{ex}} = 20 - 50 \text{ K}$.

Our ^{12}CO map suggests that we identified the outflow lobes driven by about five embedded sources in the central part of L1641-N, the mean outflow momentum for a single

outflow may be estimated to be about $80/5 = 16M_{\odot} \text{ km s}^{-1}$. If we assume the median stellar mass of $0.5 M_{\odot}$, then this gives the outflow momentum per unit stellar mass of about 32 km s^{-1} , corresponding to the nondimensional parameter f of about 0.32, which gauges the strength of an outflow, where the wind velocity of 100 km s^{-1} is adopted. This value is consistent with the fiducial values adopted by Matzner & McKee (2000), Li & Nakamura (2006), and Nakamura & Li (2007).

5. Discussion

5.1. Triggered Formation of Dust Filaments

As shown in Section 4, some dust filaments are located near the cloud edge where the ^{12}CO emission drops sharply, rather than along the ridge of the parent filamentary cloud (i.e., filaments A and E). The dust continuum emission associated with the filaments also tend to have very steep gradients in the envelopes of the filaments, in particular for the filament B. In addition, the dust filaments have two-components with different velocities. The velocity difference between the two components is significantly larger than the typical local turbulent speed. According to the line-width-size relation obtained by Heyer & Brunt (2004), the typical turbulent velocity is estimated to be around 1 km s^{-1} , about 3 times smaller than the velocity difference observed in the dust filaments. Thus, it is unlikely that the filaments were created by the dynamical compression due to the local turbulent flow. From these observational facts, we here propose that the dust filaments in this region were created by external compression, instead of the spontaneous gravitational contraction.

On the larger scale of around 10 pc, there is a significant velocity gradient along the parent filamentary cloud. The cloud component with velocities smaller than about 6 km s^{-1} is dominant in the southern part of the parent filamentary cloud, whereas the component

with velocities larger than about 7 km s^{-1} is dominant in the northern part (see Figure 6 and Figure 2 of Bally et al. 1987). The interaction between the two-components is likely to have created the filaments A, B, C, and D in this region. Here, we refer to such a possible dynamical interaction as a cloud-cloud collision. Since the two components tend to overlap toward the dust filaments on the plane of the sky (see Figures 7(b), 7(c), 8(b), and 8(c)), the collision may have occurred almost along the line of sight. The collision may also have triggered star formation in the L1641-N cluster as well as the formation of the massive filament C. The cluster formation triggered by a cloud-cloud collision have been recently discussed by several authors for other star-forming regions (Xue & Wu 2008; Furukawa et al. 2009; Duarte-Cabral et al. 2010, 2011; Galvan-Madrid et al. 2010; Higuchi et al. 2010).

Besides the possible cloud-cloud collision, other parts of this region appear to have a velocity structure that is in good agreement with an expanding motion created by a shell. A typical example is the filament E that has two velocity components inside the shell A1 but appears to converge into a single velocity component at the outer part (see Figures 7(e) and 8(e)). Such an arc-like structure in the position-velocity diagrams can be interpreted as an expanding motion of the shell. The filament C, the most massive filament, also has such an arc-like structure in the position-velocity diagram in the western side (Figure 8(c)). This massive filament may have recently been compressed by an expanding shell after it was created by the cloud-cloud collision and the cluster formation was initiated. The compression due to the expanding shell may have accelerated the recent star formation in the L1641-N cluster. We don't think that the filaments A, B, C, and D were created by the expanding shells created by the stellar feedback from the protoclusters because their main axes tend to cross the shells and they appear more or less straight, rather than curved like the filament E.

Hence, the cloud-cloud collision and the expanding shells appear to have influenced the cloud structure and kinematics in this region. In Sections 5.2 and 5.3, we discuss these two dynamical events, the cloud-cloud collision and the expanding shell, in detail.

5.2. Cloud-Cloud Collision

According to our CO channel maps, the two-components with velocities of $4 - 6 \text{ km s}^{-1}$ and $7 - 12 \text{ km s}^{-1}$ appear to be interacting to form the dense filaments. The interpretation is consistent with the previous ^{13}CO ($J = 1 - 0$) observations which suggested that two or more different velocity components are associated with the Orion A giant molecular cloud complex (Bally & Langer 1987; Bally 1989). The velocity difference between the two-components is about 3 km s^{-1} , corresponding to the Mach number of 10 under the assumption that the gas temperature is 20 K. The supersonic collision between the two-components would have increased the local density by a factor of 10^2 if the shock is isothermal. Therefore, such a shock can create the dense filaments whose densities are as large as 10^{4-5} cm^{-3} from preshock gas with 10^{2-3} cm^{-3} . In addition, the shock crossing time is estimated to be a few $\times 10^5 - 10^6 \text{ yr}$ when the typical size of the filaments is adopted as a few pc. The estimated shock crossing time is shorter than the lifetime of the L1641-N cluster (a few $\times 10^6 \text{ yr}$, see, e.g., Hodapp & Deane (1993) and Galfalk & Olofsson (2008)) by a factor of a few. Consequently, it is possible for such a collision to have triggered star formation in the dense filaments of this area. Since the shock crossing time is somewhat shorter than the lifetime of the cluster, the filament is expected to be in the postshock stage in which the observed two components may be passing over, thus leaving away from each other. According to Sakamoto et al. (1997), the blueshifted component is extended over the larger low-density area toward the eastern part of the cloud. This fact suggests that the collision with large clouds or flows (1–10 pc), instead of the collision with smaller

clouds, may have occurred. The dynamical interaction with such external flow has been recently suggested by Shimajiri et al. (2011) for the northern area of the Orion A giant molecular cloud complex. The diffuse blueshifted component found from our ^{12}CO data may be related to the flow pointed out by Shimajiri et al. (2011).

Recently, an interesting scenario on the formation of the Orion A giant molecular cloud complex has been proposed by Hartmann & Burkert (2007) who performed two-dimensional numerical simulations of gravitational collapse of a thin gas sheet. According to their model, two large filaments are first created near the edge of the gas sheet by the gravitational effects of the cloud edge where the gravitational potential takes its local minimum (see also Larson 1976 and Bastien 1983 for the effect of the cloud edge on the gravitational fragmentation). They demonstrated how an elongated rotating gas sheet with a density gradient along the major axis can gravitationally collapse to produce a structure qualitatively resembling the whole Orion A giant molecular cloud complex, having a fan-shaped structure at the southern part, ridges along the fan, and a narrow integral shaped filament at the northern part. In their model, our observed area, L1641-N, is located at the intersection between the fan and the narrow main filament, where the two large filaments collide with each other. Such a large scale interaction might be able to explain the origin of the dust filaments, although it remains unclear how the hypothetical parent gas sheet was created.

5.3. Parsec-Scale CO Shells and Protocluster Winds

As shown in Figure 9, our CO map revealed that several shells appear to shape the cloud structure in this region. The radii of the circles are about $10'$ – $20'$, corresponding to about 1–2 pc at a distance of 400 pc. Interestingly, the centers of the circles A1, A2, and A3 are close to the L1641-N cluster center, and those of the circles B1, B2, and B3 to the V 380 Ori center. Such large shells are unlikely to form by stellar feedback from a single young

star unless it is massive. Since the spectral types of the most massive cluster members are late B or early A for the two clusters, the shells may be difficult to create only by the stellar feedback of the most massive stars. Therefore, we suggest that these parsec-scale shells were created by multiple winds and/or outflows from cluster member YSOs. The reason why three or more shells are associated with each cluster remains unclear. One possibility is that the total momentum injection rate from cluster member YSOs is not constant but episodic because the star formation rate is likely to fluctuate or oscillate with time. Another possibility is that these circles represent dense parts of an expanding shell that is propagating into inhomogeneous media. Here, we call these YSO winds as “protocluster wind.” In the next subsection, we consider the dynamical evolution of the shell driven by the protocluster wind, using a simple analytic model.

Kinematical evidence that the protocluster wind is responsible for the cloud dynamical evolution comes from the filament E that is located at the western edge of the cloud and has an arc-like shape. The filament E has two velocity components inside the circle A1 but appears to converge into a single velocity component at the outer part (see Figures 7(e) and 8(e)), as mentioned in Section 5.1. It is also distributed along the circle A1 whose center coincides with the L1641-N cluster, suggesting that it may have been created by the shell driven by the protocluster wind from the L1641-N cluster.

Another example of the parsec-scale expanding shell is the one whose center is close to V 380 Ori. This shell is fully covered by the ^{13}CO ($J = 1 - 0$) map obtained by Bally & Langer (1987), although the southern part of the shell is not covered by our ^{12}CO data. We show in the ^{13}CO integrated intensity map presented in Figure 12 the circles that appear to fit the shells. The ^{13}CO position-velocity diagrams of the shells toward the two positions (Figures 8(d) and 8(f)) clearly show the existence of the two different velocity components, consistent with the expanding motion. The expanding motion of the shell is

in good agreement with Heyer et al. (1992) who found a similar expanding motion of the shell.

5.4. Expanding Motions Driven by Protocluster Winds

In the following, we discuss how the protocluster wind evolves in the parent molecular cloud using a simple analytic model. Here, we consider the motion of an expanding shell driven by protostellar winds from cluster member YSOs in a uniform media with density ρ_0 . For simplicity, we don't take into account the effects of protostellar outflows in the following calculations, but discuss the effect of the protostellar outflow feedback in the next subsection.

If a wind from a protostar with a radius R_* is driven by a ram pressure $\rho_w V_w^2$, then the motion of an expanding shell is described as

$$\frac{d}{dt} \left(\frac{4\pi}{3} R^3 \rho_0 \frac{dR}{dt} \right) = \sum_{i=1}^N 4\pi R_*^2 \rho_w V_w^2 \quad (1)$$

where ρ_w is the wind density, V_w is the wind velocity, R is the radius of the shell, and N is the number of YSOs. For simplicity, all the stars are assumed to inject the wind momentum simultaneously at the same constant rate. From the above equation, the time evolution of the shell radius is given by

$$\begin{aligned} R &= \left(\frac{3 \sum_{i=1}^N \dot{M} V_w}{2\pi \rho_0} \right)^{1/4} t^{1/2} \\ &\simeq 2 \text{ pc} \left(\frac{N}{100} \right)^{1/4} \left(\frac{\dot{M}}{10^{-7} M_\odot \text{ yr}^{-1}} \right)^{1/4} \left(\frac{V_w}{200 \text{ km s}^{-1}} \right)^{1/4} \\ &\quad \times \left(\frac{\rho_0}{10^3 \text{ cm}^{-3}} \right)^{-1/4} \left(\frac{t}{10^6 \text{ yr}} \right)^{1/2}, \end{aligned} \quad (2)$$

where \dot{M} is the mass loss rate from a single YSO and given by $4\pi R_*^2 \rho_w V_w$. The expanding

velocity of the shell, V_s , is evaluated as

$$\begin{aligned}
 V_s &= \frac{dR}{dt} \\
 &\simeq 1 \text{ km s}^{-1} \left(\frac{N}{100} \right)^{1/4} \left(\frac{\dot{M}}{10^{-7} M_\odot \text{ yr}^{-1}} \right)^{1/4} \left(\frac{V_w}{200 \text{ km s}^{-1}} \right)^{1/4} \\
 &\quad \times \left(\frac{\rho_0}{10^3 \text{ cm}^{-3}} \right)^{-1/4} \left(\frac{t}{10^6 \text{ yr}} \right)^{-1/2}.
 \end{aligned} \tag{3}$$

The typical mass loss rate and wind velocity from YSOs are somewhat uncertain. Some observations suggest that the mass loss rate and wind velocity from a low-mass YSO are of the order of $10^{-7} M_\odot \text{ yr}^{-1}$ and a few $\times 10^2 \text{ km s}^{-1}$, respectively (e.g., Norman & Silk 1980; Wilkin & Stahler 1998). Here, we adopted $\dot{M} = 10^{-7} M_\odot \text{ yr}^{-1}$ and $V_w = 200 \text{ km s}^{-1}$ as their representative values. For the L1641-N and V 380 Ori clusters, the number of cluster member YSOs is of the order of 100. Adopting the density of 10^3 cm^{-3} for the ambient gas and the cluster lifetimes of 10^6 yr , the radius of the expanding shell and the expansion velocity are evaluated to be about 2 pc and 1 km s^{-1} , respectively, comparable to those of the shells identified from our ^{12}CO data. Therefore, the protocluster winds from these two clusters are likely to have enough energies to produce the parsec-scale shells within a few Myr.

5.5. Molecular Outflows in the L1641N cluster

In the previous subsection, we omitted the contribution of the outflow feedback on the dynamical evolution of the expanding shell. However, recent numerical simulations of cluster formation have suggested that protostellar outflow feedback plays an important role in regulating star formation in cluster-forming clumps because they inject substantial amount of kinetic energy into the surroundings (Li & Nakamura 2006; Nakamura & Li 2007; Carroll et al. 2009; Wang et al. 2010). In addition, the propagation directions of

the collimated outflows in the clustered environment are not so aligned preferentially in the global magnetic field direction even in the presence of a strong magnetic field (Nakamura & Li 2011). Therefore, the total outflow momentum is expected to be injected isotropically on average. Here, we attempt to assess how the outflow feedback of the L1641-N cluster influences the surrounding gas and contributes to the dynamical evolution of the expanding shell.

5.5.1. *Dynamical State of the L1641-N Cluster Forming Clump*

Recently, Nakamura et al. (2011b) investigated how molecular outflow feedback influences the dynamical state of a nearby cluster-forming clump, Serpens South, by applying the virial analysis. They found that the Serpens South clump is close to virial equilibrium and the total kinetic energy injected by the current outflow activity is less than the clump gravitational energy, concluding that the current outflow activity is not enough to destroy the whole cluster-forming clump. In the following, we follow Nakamura et al. (2011b) and clarify how the current outflow activity in the L1641-N cluster impacts the whole clump.

The virial equation for a spherical clump is given by

$$\frac{1}{2} \frac{\partial^2 I}{\partial t^2} = 2U + W, \quad (4)$$

where the terms, I , U , and W , denote the moment of inertia, internal kinetic energy, and gravitational energy, respectively. Here, we neglect the surface pressure term. A clump is in virial equilibrium when the right-hand-side of Equation (4) is zero, i.e., $2U + W = 0$. The kinetic energy and gravitational energy terms are expressed, respectively, as

$$U = \frac{3M\Delta V^2}{16 \ln 2} \quad (5)$$

and

$$W = -a \frac{GM^2}{R} \left[1 - \left(\frac{\Phi}{\Phi_{\text{cr}}} \right)^2 \right], \quad (6)$$

where M is the clump mass, ΔV is the 1D FWHM velocity width, G is the gravitational constant, R is the radius of the clump, the values Φ and Φ_{cr} are, respectively, the magnetic flux penetrating the clump and the critical magnetic flux above which the magnetic field can support the clump against the self-gravity. Although according to recent observations of magnetic fields associated with the nearby parsec-scale cluster-forming clumps, the values of Φ/Φ_{cr} are estimated to be around 0.5 (e.g., Falgarone et al. 2008; Sugitani et al. 2010, 2011; Kwon et al. 2011), we here neglect the effect of the magnetic support for simplicity (i.e., $\Phi = 0$). The dimensionless parameter, a , measures the effects of a nonuniform and/or nonspherical mass distribution (Bertoldi & McKee 1992), and is of the order unity. For a uniform sphere and a centrally-condensed sphere with $\rho \propto r^{-2}$, $a = 3/5$ and 1, respectively. Here, we adopt $a = 1$ because the cluster-forming clump tends to be centrally condensed.

According to Stanke & Williams (2007), the radius and mass of the cluster-forming clump associated with the L1641-N cluster are roughly estimated to be 0.5 pc and $150 M_{\odot}$, respectively. Here, only the part involved in directly building the L1641-N cluster, i.e., a head of the clump, is defined as the cluster-forming clump, although the parent clump has a long tail extending southeast of the L1641-N cluster, as shown in the 1.1 mm map. The 1D FWHM velocity width is estimated at about 2 km s^{-1} from the ^{12}CO data. Using these values, the kinetic energy and gravitational energy terms are estimated to be $2U \simeq 325 M_{\odot} \text{ km}^2 \text{ s}^{-2}$ and $W \simeq -194 M_{\odot} \text{ km}^2 \text{ s}^{-2}$, respectively. These values are comparable to the estimate by Stanke & Williams (2007) who conducted a similar analysis using their ^{12}CO ($J = 2 - 1$) data. Thus, the clump is likely to be close to virial equilibrium or somewhat gravitationally unbound. On the other hand, the total kinetic energy due to the outflows is evaluated at $E_{\text{out}} \simeq 273 M_{\odot} \text{ km}^2 \text{ s}^{-1}$. This is comparable to the clump gravitational energy. Although the substantial amount of the outflow kinetic energy appears to escape from the

clump, the energy input due to the current outflow activity seems to influence the clump dynamics significantly.

5.5.2. *Effects of the Molecular Outflows on the Expanding Shells*

As shown in Figure 11, the identified outflow lobes often extend beyond the dense clump traced by the dust continuum emission, implying that the outflow momentum escaped from the clump is likely to influence the density and velocity structure in the surroundings. If the escaped momentum flux is about a half the total injected outflow momentum flux, it is estimated to be about $10^{-3}M_{\odot} \text{ km s}^{-1} \text{ yr}^{-1}$, assuming the outflow dynamical time of a few $\times 10^4$ yr. On the other hand, the total momentum flux injected from the protostellar winds is estimated to be $N\dot{M}V_w \simeq 100 \times 10^{-7} \times 200 = 2 \times 10^{-3}M_{\odot} \text{ km s}^{-1} \text{ yr}^{-1}$, where we adopted the values given in Equations (2) and (3). The estimated wind momentum flux is comparable to that of the protostellar outflow feedback. Therefore, we conclude that both the protostellar outflow and wind feedback can contribute to the dynamical evolution of the expanding shell created by the protocluster wind from the L1641-N cluster. However, the weak dependence on the injected momentum in Equations (2) and (3) indicates that even if we take into account both the protostellar outflows and winds, the estimated radius and expanding velocity of the shell do not change significantly.

6. Summary

We carried out the ^{12}CO ($J = 1 - 0$) mapping observations toward the $48' \times 48'$ area including the L1641-N cluster in the Orion A giant molecular cloud complex, using the Nobeyama 45 m telescope. The main results are summarized as follows.

1. From comparison between the ^{12}CO ($J = 1 - 0$) map and the 1.1 mm continuum

image, we found that several dust filaments are located near the cloud edge traced by the ^{13}CO ($J = 1 - 0$) emission.

2. The dust filaments have two-components with different velocities. The velocity difference between the two-components is about 3 km s^{-1} , which is significantly larger than the typical local turbulent speed of 1 km s^{-1} . Therefore, we suggest that the dust filaments were created by the dynamical compression triggered externally, i.e., a cloud-cloud collision, instead of the spontaneous gravitational contraction.

3. The ^{12}CO ($J = 1 - 0$) and ^{13}CO ($J = 1 - 0$) velocity channel maps suggest that the blueshifted ($V_{\text{LSR}} \lesssim 6 \text{ km s}^{-1}$) and redshifted ($V_{\text{LSR}} \gtrsim 7 \text{ km s}^{-1}$) components are interacting with each other. Since the two components appear to overlap toward the dust filaments on the plane of the sky, the collision between the two components may have occurred almost along the line of sight. A good example of such a cloud-cloud collision is the most massive dust filament, associated with the L1641-N cluster, which has the two-components with different velocities at the long tail stretching from the head of the dust filament. We suggest that the formation of the L1641-N cluster may have been triggered by such a collision. Since the shock crossing time is somewhat shorter than the lifetime of the L1641-N cluster, the massive filament associated with the cluster may be in the postshock stage in which the two components with the different velocities are passing over, thus leaving away from each other.

4. We found several parsec-scale shells in the ^{12}CO ($J = 1 - 0$) data cube. Some of the shells appear to be spatially well-ordered and homocentric. The centers of the shells are close to either the L 1641-N or V 380 Ori cluster centers, implying that the star formation activity in the clusters may be responsible for the formation and evolution of the shells. In particular, the shell surrounding V 380 Ori is prominent in the ^{13}CO map.

5. The molecular gas distribution and kinematical structure of this region led us

to the following scenario. On the large scale of at least about $1 - 10$ pc, a cloud-cloud collision may have occurred almost along the line of sight in this region, contributing to the formation of several dense filaments (the filaments A through D). The cloud-cloud collision have triggered the formation of the L1641-N cluster. Multiple protostellar winds and outflows from the cluster member YSOs created large expanding bubbles that can be recognized in the ^{12}CO and ^{13}CO maps. Here, we call these YSO winds as “protocluster winds.” The dust filament located at the western cloud edge (filament E) appears to curve along the shell whose center is the L1641-N cluster, and have two different velocity components at the inner part of the shell. The two components appear to converge into a single velocity component at the outer part of the shell. It is consistent with an idea that the filament E is a part of the expanding shell created by the protocluster wind from the L1641-N cluster. The shell surrounding V 380 Ori also has two different velocity components both in the ^{12}CO and ^{13}CO maps, reaching the filament C. It presumably hit the filament C, influencing the recent star formation in the L1641-N cluster. Both the cloud-cloud collision and the protocluster winds are likely to have created the complicated cloud morphology and kinematics in this region.

6. Toward the L1641-N cluster, we identified a number of the outflow lobes using the ^{12}CO ($J = 1 - 0$) data. The identified lobes are reasonably in good agreement with the results of Stanke & Williams (2007) who identified the outflow lobes in this region with the ^{12}CO ($J = 2 - 1$) emission, using the IRAM 30 m telescope and SMA. The total outflow energy in the L1641-N cluster is comparable to the gravitational energy of the cluster-forming clump. This may suggest that the outflow feedback influences the dynamical evolution of the clump significantly. Assuming the median stellar mass of $0.5M_{\odot}$, the mean outflow momentum per unit stellar mass is estimated to be about 32 km s^{-1} , under the assumption of optically thin gas. This mean outflow momentum corresponds to the nondimensional outflow parameter of $f = 0.32$, which gauges the strength of an outflow.

This value of f is comparable to the fiducial values of $f = 0.4$ adopted by Matnzer & McKee (2000), Li & Nakamura (2006), and Nakamura & Li (2007).

This work is supported in part by a Grant-in-Aid for Scientific Research of Japan (20540228, 22340040). We thank John Bally for kindly giving us the ^{13}CO ($J = 1 - 0$) fits data of the Orion A giant molecular cloud complex taken by the 7 m telescope of AT&T Bell Laboratories. We are grateful to Henrik Beuther, Christopher J. Davis, M. S. Nanda Kumar, and Christopher F. McKee for their valuable comments. This work was carried out as one of the projects of the Nobeyama Radio Observatory (NRO), which is a branch of the National Astronomical Observatory of Japan, National Institute of Natural Sciences. We also thank the NRO staff for both operating the 45 m and helping us with the data reduction.

REFERENCES

- Allen, L. E. & Davis, C. J. 2008, in Handbook of Star Forming Regions Vol. 1, eds. Bo Reipurth, (Astro. Soc. of Pacific), p. 621
- Arce, H. G., Borkin, M. A., Goodman, A. A., et al. 2010, ApJ, 715, 1170
- Baines, D., Oudmaijer, R. D., Porter, J. M., & Pozzo, M. 2006, MNRAS, 367, 737
- Bally, J. & Langer, W. D. 1987, ApJ, 312, L45
- Bally, J. 1989, in Proc. ESO Workshop on Low-Mass Star Formation and Pre-Main-Sequence Objects, ed. B. Reipurth (Garching: ESO), p. 1
- Bally, J., Langer, W. D., & Liu, W. 1991, ApJ, 383, 645
- Bally, J. 2008, in Handbook of Star Forming Regions Vol. 1, eds. Bo Reipurth, (Astro. Soc. of Pacific), p. 459
- Banerjee, R., Vazquez-Semadeni, E., Hennebelle, P., & Klessen, R. S. 2009, MNRAS, 398, 1082
- Bastien, P. 1983, A&A, 119, 109
- Bertoldi, F., & McKee, C. F. 1992, ApJ, 395, 140
- Bontemps, S., André, P., Terebey, S., & Cabrit, S. 1996, A&A, 311, 858
- Carpenter, J. M., Hillenbrand, L. A., & Skrutskie, M. F. 2001, AJ, 121, 316
- Carroll, J. J., Frank, A., Blackman, E. G., et al. 2009, ApJ, 695, 1376
- Davis, C. J., Froebrich, D., Stanke, T., et al. 2009, A&A, 496, 153
- Duarte-Cabral, A., Fuller, G. A., Peretto, N., et al. 2010, A&A, 519, 27 2011, ApJ, 528, 50

- Duarte-Cabral, A., Dobbs, C. L., Peretto, N., & Fuller, G. A. 2011, *ApJ*, 528, 50
- Falgarone, E., Troland, T. H., Crutcher, R. M., & Paubert, G. 2008, *A&A*, 487, 247
- Fang, M., van Boekel, R., Wang, W., et al. 2008, *A&A*, 504, 461
- Fukui, Y., Sugitani, K., Takaba, H., et al. 1986, *ApJ*, 311, L85
- Fukui, Y., Takaba, H., Iwata, T., & Mizuno, A. 1988, *ApJ*, 325, L13
- Furukawa, N., Dawson, J. R., Ohama, A., et al. 2009, *ApJ*, 696, L115
- Galfalk, M. & Olofsson, G. 2008, *A&A*, 489, 14090
- Galvan-Madrid, R., Zhang, Q., Keto, E., et al. 2010, *ApJ*, 725, 17
- Gritschneider, M., Naab, T., Walch, S., et al. 2009, *ApJ*, 694, 26
- Hartmann, L., & Burkert, A. 2007, *ApJ*, 654, 988
- Heyer, M. H., Morgan, F. P., Schloerb, R. L., et al. 1992, *ApJ*, 395, L99
- Heyer, M. H., & Brunt, C. M. 2004, *ApJ*, 615, L45
- Higuchi, A. E., Kuroono, Y., Saito, M., & Kawabe, R. 2010, *ApJ*, 719, 1813
- Hirota, T., Ando, K., Bushimata, T., et al. 2008, *PASJ*, 60, 961
- Hodapp, K. & Deane, J. 1993, *ApJS*, 88, 119
- Ikeda, N., Sunada, K., & Kitamura, Y. 2007, *ApJ*, 665, 1194
- Krumholz, M. R., Klein, R. I., McKee, C. F. 2011, *ApJ* in press
- Kwon, J., Tamura, M., Kandori, R., et al. 2011, *ApJ*, in press (arXiv1108.2341)
- Larson, R. B. 1976, *MNRAS*, 156, 437

- Li, Z.-Y., & Nakamura, F. 2006, *ApJ*, 640, L187
- Mac Low, M.-M., & Klessen, R. S. 2004, *Rev. Mod. Phys.*, 76, 125
- Matzner, C. D. & McKee, C. F. 2000, *ApJ*, 545, 364
- McKee, C. F., & Ostriker, E. C. 2007, *ARA&A*, 45, 565
- Menten, K. M., Reid, M. J., Forbrich, J., & Brunthaler, A. 2007, *A&A*, 474, 515
- Nakamura, F., & Li, Z.-Y. 2007, *ApJ*, 662, 395
- Nakamura, F., & Li, Z.-Y. 2011, *ApJ*, 740, 36
- Nakamura, F., Kamada, Y., Kamazaki, T., et al. 2011a, *ApJ*, 726, 46
- Nakamura, F., Sugitani, K., Shimajiri, Y., et al. 2011b, *ApJ*, 737, 56
- Norman, C., & Silk, J. 1980, *ApJ*, 238, 158
- O’Dell, C. R., Muench, A., Smith, N., & Zapata, L. 2008, in *Handbook of Star Forming Regions*, Vol. 1, eds. Bo Reipurth, (Astro. Soc. of Pacific), p. 544
- Rebull, L. M., Stauffer, J. R., Megeath, T. S., et al. 2006, *ApJ*, 646, 297
- Sakamoto, S., Hasegawa, T., Hayashi, M., et al. 1997, *ApJ*, 481, 302
- Sandell, G. & Knee, L. B. G. 2001, *ApJ*, 546, L49
- Sandstrom, K. M., Peek, J. E. G., Bower, G. C., et al. 2007, *ApJ*, 667, 1161
- Shimajiri, Y., Takahashi, S., Takakuwa, S., et al. 2008, *ApJ*, 683, 255
- Shimajiri, Y., Kawabe, R., Takakuwa, S., et al. 2011, *PASJ*, 63, 105
- Stanke, T. & Williams, J. P. 2007, *AJ*, 133, 1307

- Strom, K. M., Strom, S. E., & Merrill, K. M. 1993, *ApJ*, 412, 233
- Sugitani, K., Nakamura, F., Tamura, M., et al. 2010, *ApJ*, 716, 299
- Sugitani, K., Nakamura, F., Watanabe, M., et al. 2011, *ApJ*, 734, 63
- Takahashi, S., Saito, M., Ohashi, N., et al. 2008, *ApJ*, 688, 344
- Tatematsu, K., Umemoto, T., Murata, Y., et al. 1993, *ApJ*, 404, 643
- Vazquez-Semadeni, E., Colin, P., Gomez, G. C., et al. 2010, *ApJ*, 715, 1302
- Wang, P., Li, Z.-Y., Abel, T., & Nakamura, F. 2010, *ApJ*, 709, 27
- Wilkin, F. P., & Stahler, S. W. 1998, *ApJ*, 502, 661
- Wilking, B. A., Blackwell, J. H., & Mundy, L. G. 1990, *AJ*, 100, 758
- Xue, R. & Wu, Y. 2008, *ApJ*, 680, 446

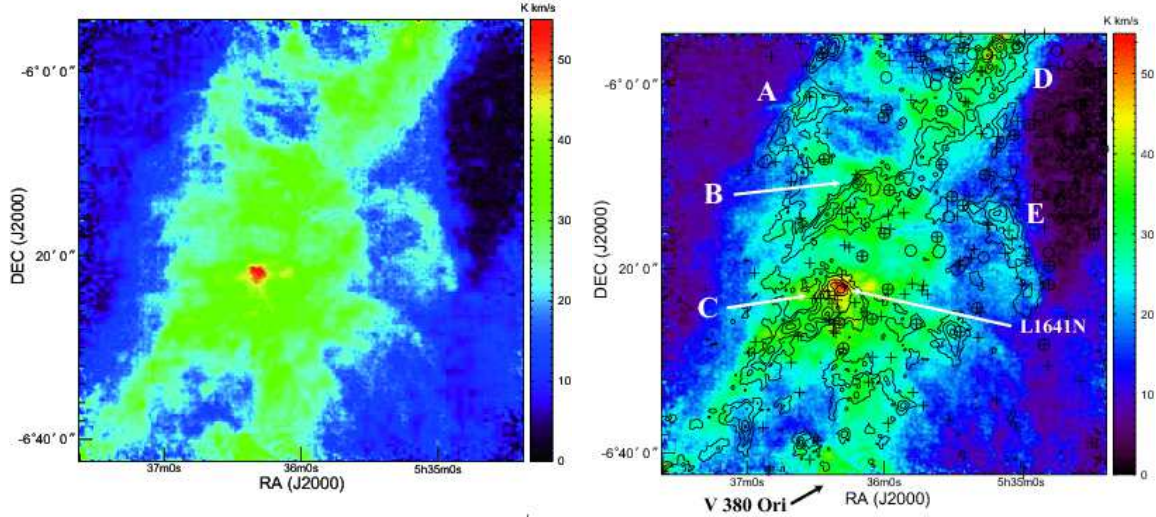


Fig. 1.— (a) ^{12}CO ($J = 1 - 0$) total integrated intensity map in the velocity range from $v_{\text{LSR}} = 0.0$ to 20.0 km s^{-1} toward the $48' \times 48'$ area including the L1641-N cluster. The effective spatial resolution of the map is $21''$. The ^{12}CO emission peak coincides reasonably well with the position of the L1641-N cluster. (b) Same as panel (a), but the 1.1 mm continuum data are overlaid on the ^{12}CO ($J = 1 - 0$) total integrated intensity map. The contours are drawn at 0.06, 0.15, 0.3, 0.6, and 1.2 Jy/beam. The 1σ rms noise level is 9 mJy/beam. The positions of YSOs identified by Rebull et al. (2006) and Carpenter et al. (2001) are overlaid on the images by the circles and crosses, respectively. Note that the plotted YSOs are less embedded sources, and therefore younger embedded YSOs are not shown. Several dust filaments are labeled with alphabet A through E. The positions of L1641-N and V 380 Ori are indicated by the white arrows.

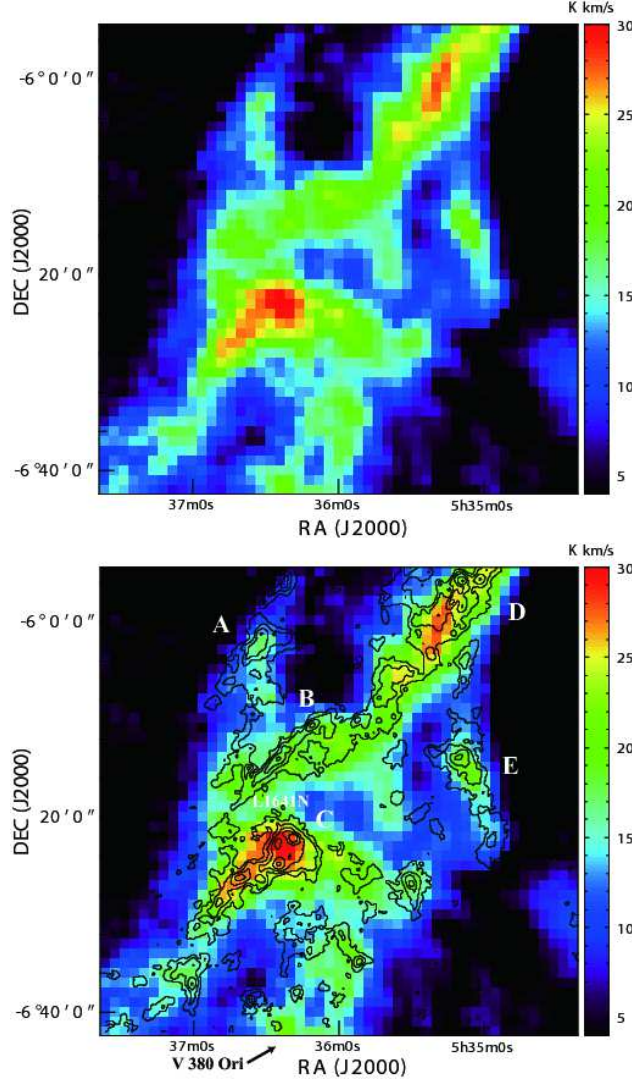


Fig. 2.— (a) ^{13}CO ($J=1-0$) total integrated intensity map toward the same area presented in Figure 1 in the velocity range from $v_{\text{LSR}} = 1.0$ to 14.0 km s^{-1} . The ^{13}CO data were obtained by Bally & Langer (1987) with the 7 m AT&T Bell laboratories telescope. The strongest ^{13}CO emission is associated with the L1641-N cluster. (b) Same as panel (a) but the 1.1 mm continuum data are overlaid with the contours on the ^{13}CO ($J=1-0$) total integrated intensity map. The contours are drawn at 0.06, 0.15, 0.3, 0.6, and 1.2 Jy/beam. Several dust filaments are labeled with alphabet A through E.

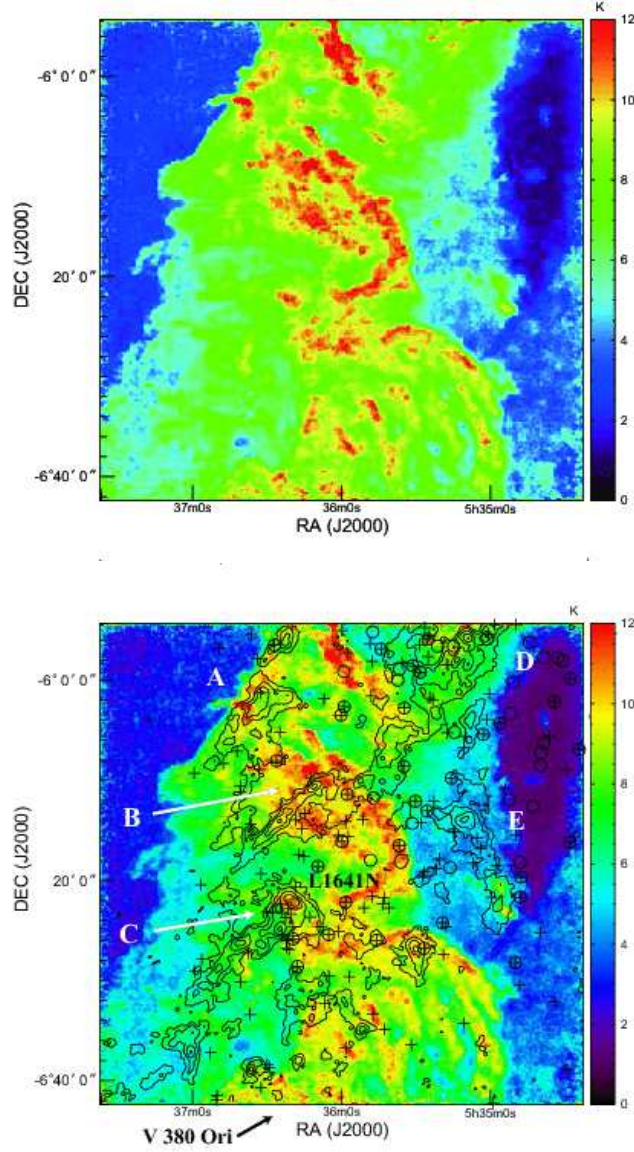


Fig. 3.— (a) ^{12}CO ($J = 1 - 0$) peak intensity map. (b) Same as panel (a) but the 1.1 mm continuum contours are overlaid. The contours are drawn at 0.06, 0.15, 0.3, 0.6, and 1.2 Jy/beam. The crosses and circles denote the positions of YSOs identified by Spitzer (Rebull et al. 2006), respectively. Note that these YSOs are less embedded sources. Several dust filaments are labeled with alphabet A through E.

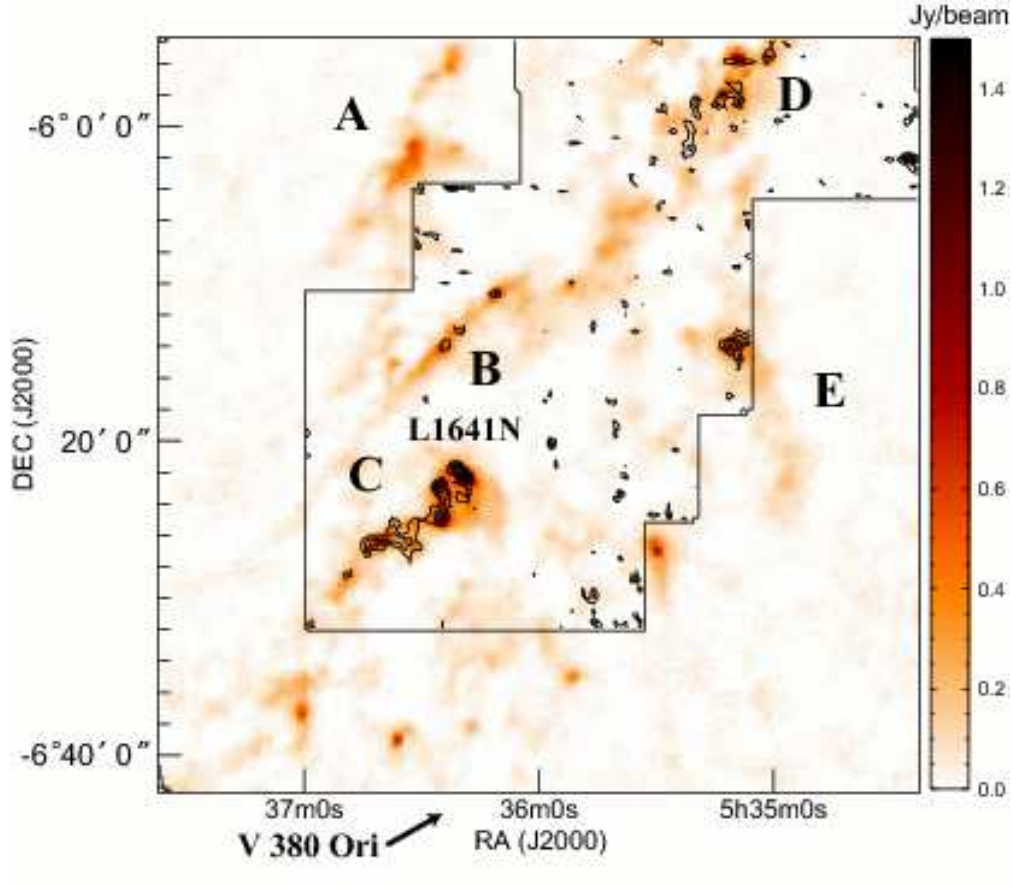


Fig. 4.— H^{13}CO^+ ($J = 1 - 0$) velocity integrated intensity contours overlaid on the 1.1 mm dust continuum image taken by AzTEC on ASTE. The velocity range is from $v_{\text{LSR}} = 4.0$ to 14.0 km s^{-1} . The contours start from 0.42 K km s^{-1} at intervals of 0.2 K km s^{-1} . The solid lines indicate the observation box for the H^{13}CO^+ ($J = 1 - 0$) emission. The data were taken from the Nobeyama 45 m archival data (<http://www.nro.nao.ac.jp/>). Several dust filaments are detected in the H^{13}CO^+ emission, indicating that they contain dense gas with 10^5 cm^{-3} . Several dust filaments are labeled by alphabet A through E.

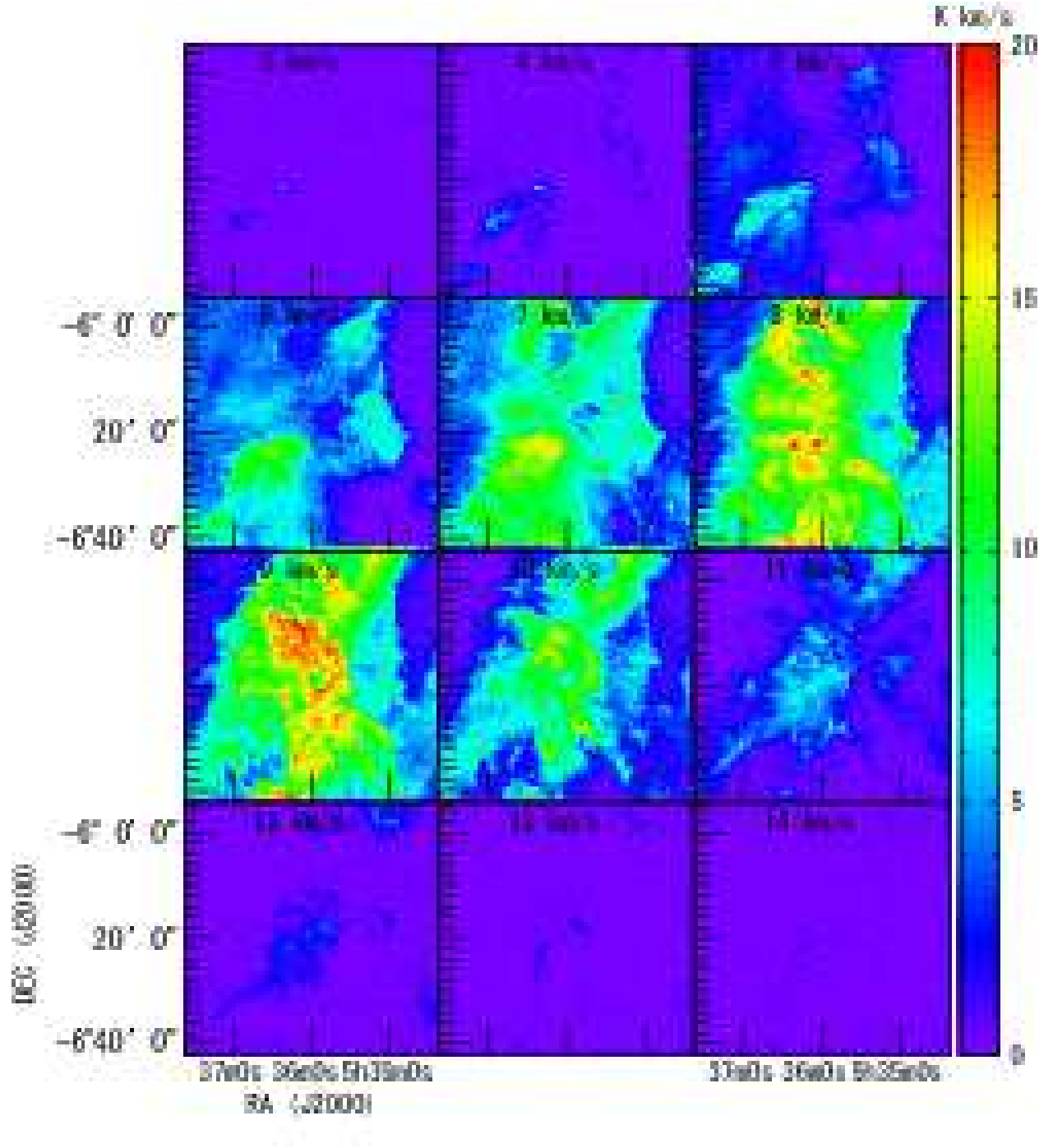


Fig. 5.— ^{12}CO ($J = 1 - 0$) velocity channel maps with velocity width of 1.0 km s^{-1} .

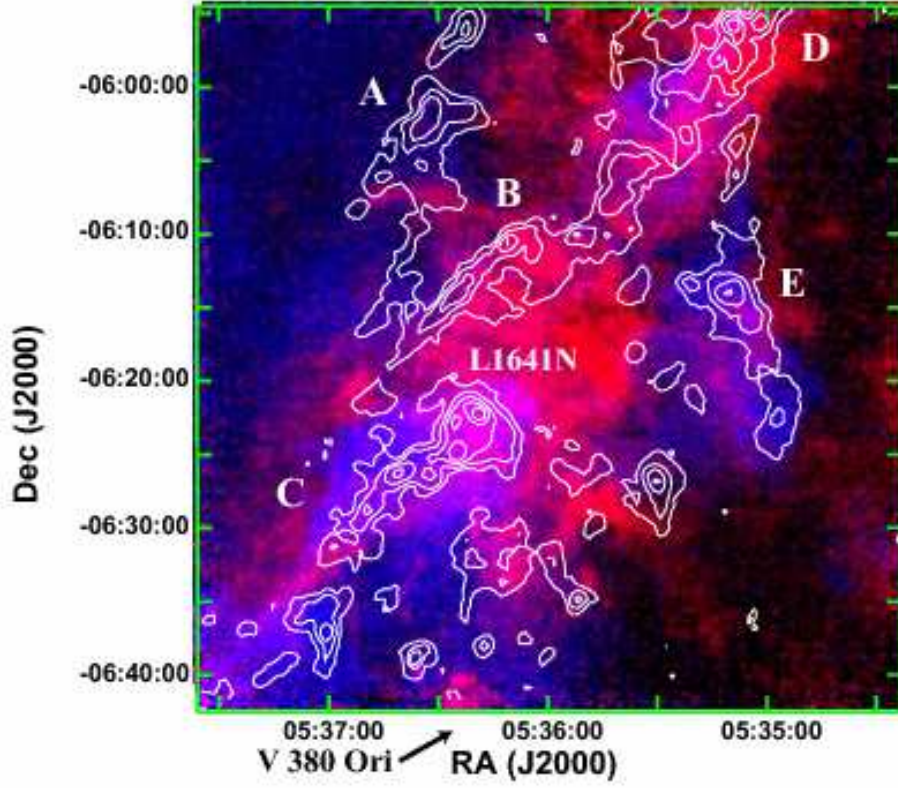


Fig. 6.— Two-color image toward the same area presented in Figure 1 with redshifted ^{12}CO ($J = 1 - 0$) integrated intensity in red ($9.5 \text{ km s}^{-1} \sim 14.5 \text{ km s}^{-1}$) and blueshifted ^{12}CO ($J = 1 - 0$) integrated intensity in blue ($3.5 \text{ km s}^{-1} \sim 6.5 \text{ km s}^{-1}$). The white contours indicate the 1.1 mm dust continuum emission at levels of 0.06, 0.15, 0.3, 0.6, and 1.2 Jy/beam.

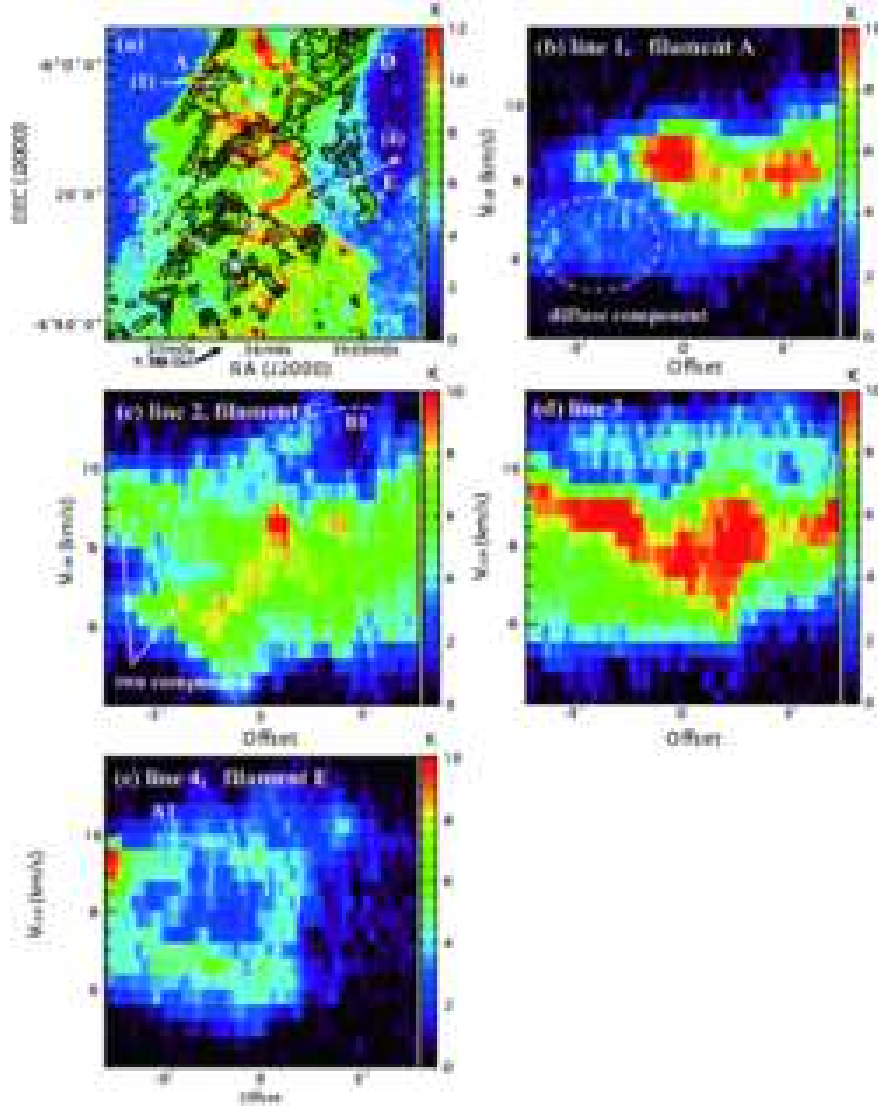


Fig. 7.— (a) ^{12}CO ($J = 1 - 0$) peak intensity map showing the positions of the PV diagrams presented in panels (b) through (e). The 1.1 mm continuum map is overlaid on the image with the black contours whose levels are the same as those of Figure 1. (b) Position-velocity diagram along the line (1). The abscissa denotes the offset measured from the position of the white cross indicated in panel (a). The plus and minus values are for the western and eastern sides of the cross. (c) Same as panel (b) but for the line (2). (d) Same as panel (b) but for the line (3). (e) Same as panel (b) but for the line (4).

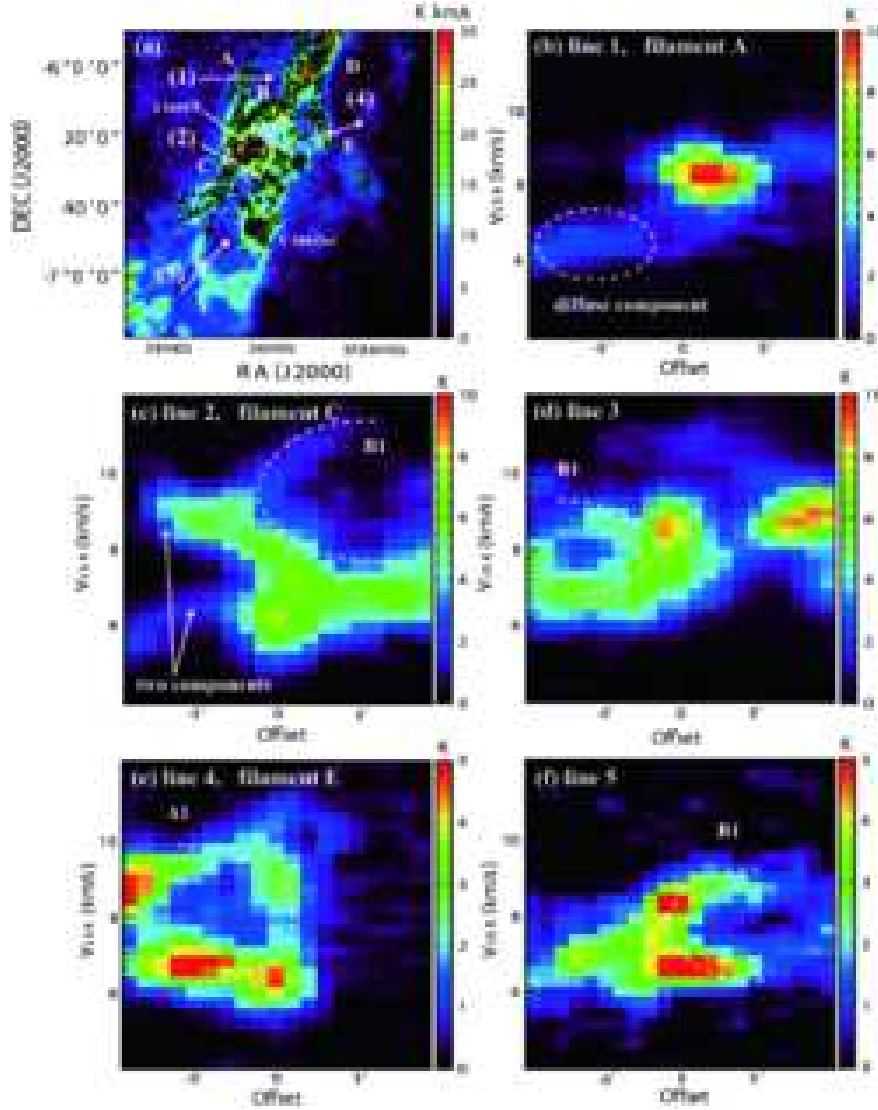


Fig. 8.— (a) ^{13}CO ($J = 1 - 0$) velocity integrated intensity map showing the positions of the PV diagrams. The velocity integration range is the same as that of 2. The lines (b) through (e) are the same as those of Figure 7. The 1.1 mm continuum map is overlaid on the image with the black contours whose levels are the same as those of Figure 1. Note that the southern part (below Dec. $\sim -6 : 30$) was not covered by the 1.1 mm observations (see Shimajiri et al. 2011) (b) Position-velocity diagram along the line (1). The velocity resolution of the data is 0.2 km s^{-1} . (c) Same as panel (b) but for the line (2). (d) Same as panel (b) but for the line (3). (e) Same as panel (b) but for the line (4). (f) Same as panel (b) but for the line (5).

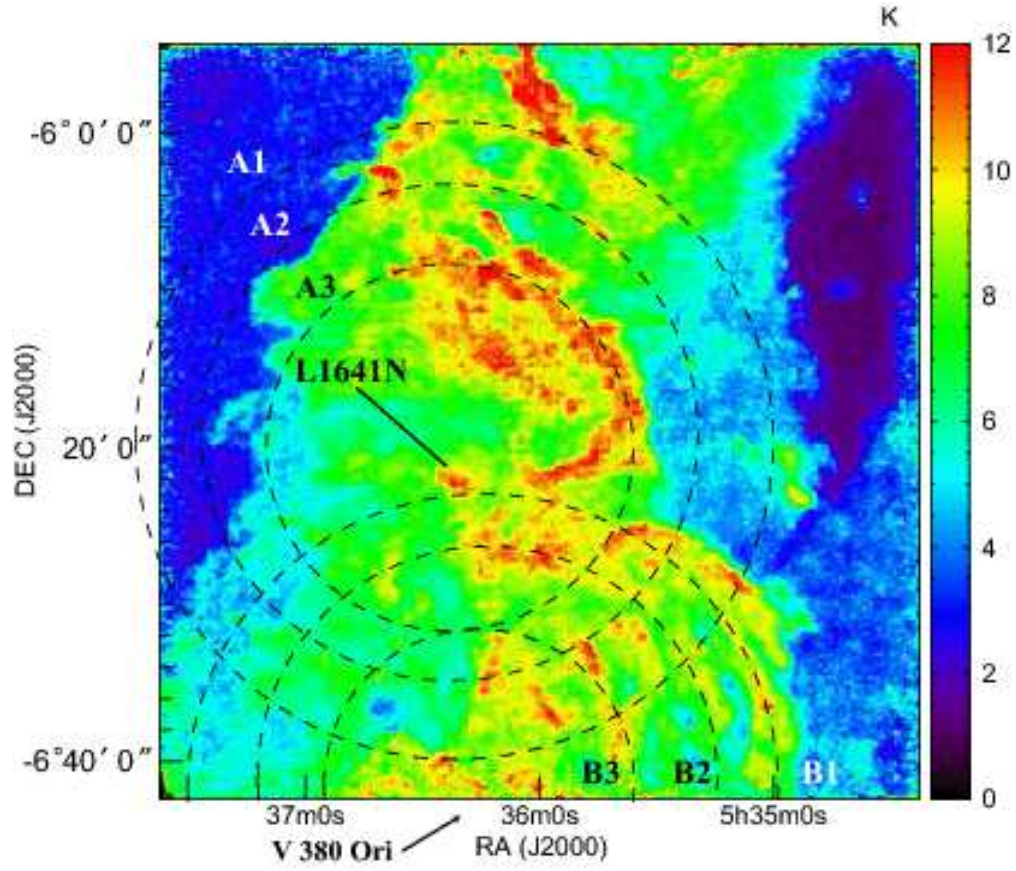


Fig. 9.— Same as Figure 3 but the positions of parsec-scale shells are indicated with the dashed lines.

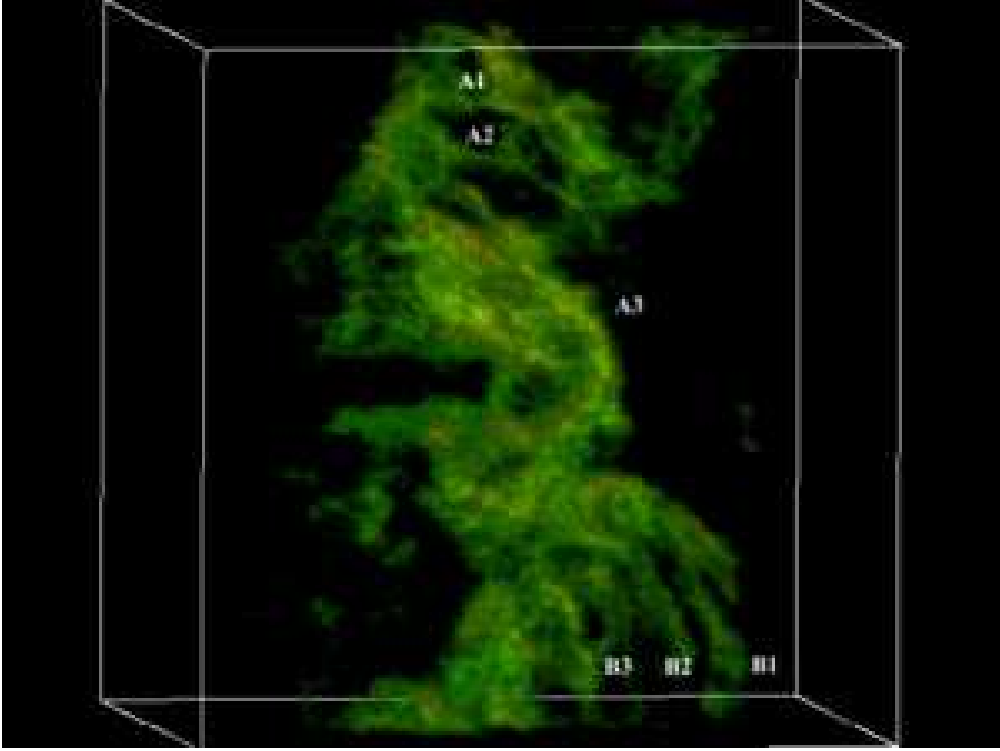


Fig. 10.— Three-dimensional representation of the antenna temperature (T_{A}^*) of the CO ($J = 1 - 0$) emission in the RA-DEC- V_{LSR} space. The green color roughly represents the parts with $T_{\text{A}}^* \sim 15$ K. Several arc-like structures can be recognized in the RA-DEC- V_{LSR} space.

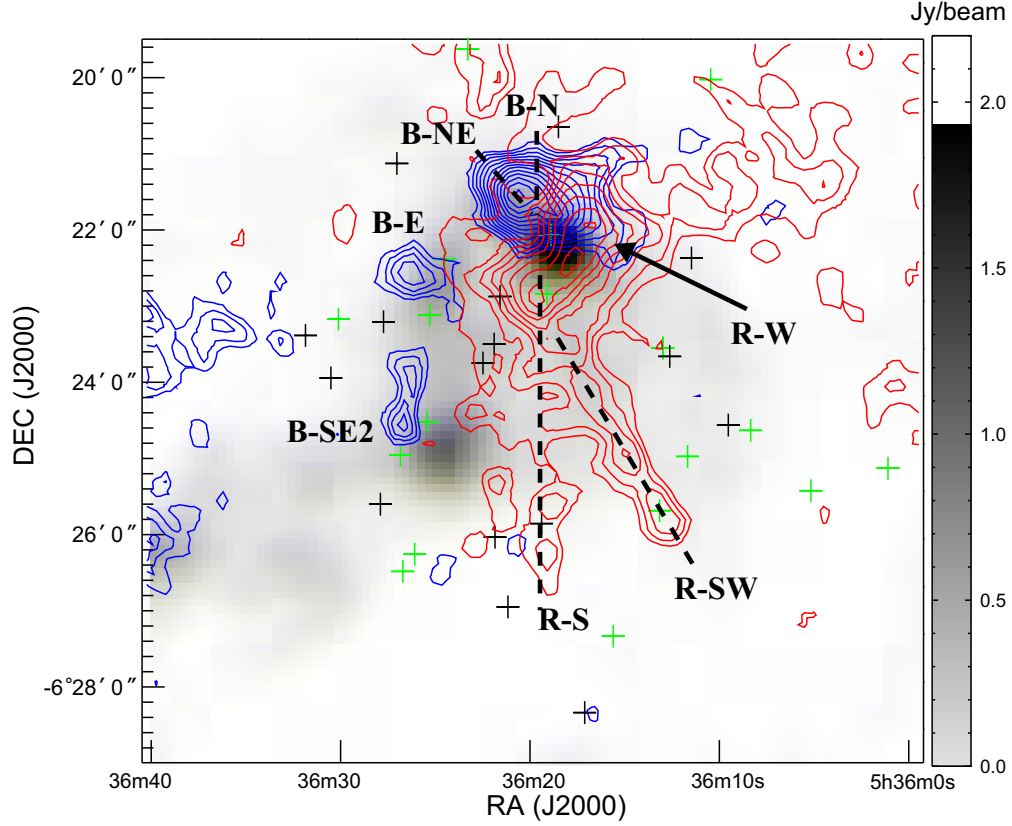


Fig. 11.— CO ($J = 1 - 0$) integrated intensity contours toward the L1641-N cluster on the 1.1 mm image obtained by Shimajiri et al. (2011). The displayed area is almost the same as that shown in Figure 2 of Stanke & Williams (2007) who mapped the same area in CO ($J = 2 - 1$). The outflow lobes seen in the CO ($J = 1 - 0$) data are also labeled following Stanke & Williams (2007). The blue contours represent blueshifted CO ($J = 1 - 0$) intensity integrated from 0.25 km s^{-1} to 5.25 km s^{-1} , starting from 5 K km s^{-1} at intervals of 0.75 K km s^{-1} . The red contours represent blueshifted CO ($J = 1 - 0$) intensity integrated from 9.75 km s^{-1} to 15.75 km s^{-1} , starting from 9 K km s^{-1} at intervals of 0.75 K km s^{-1} . The gray scale represents the 1.1 mm image in units of Jy beam^{-1} . The positions of the classical and weak-line T-Tauri stars observed by Fang et al. (2009) are shown in black and green crosses, respectively.

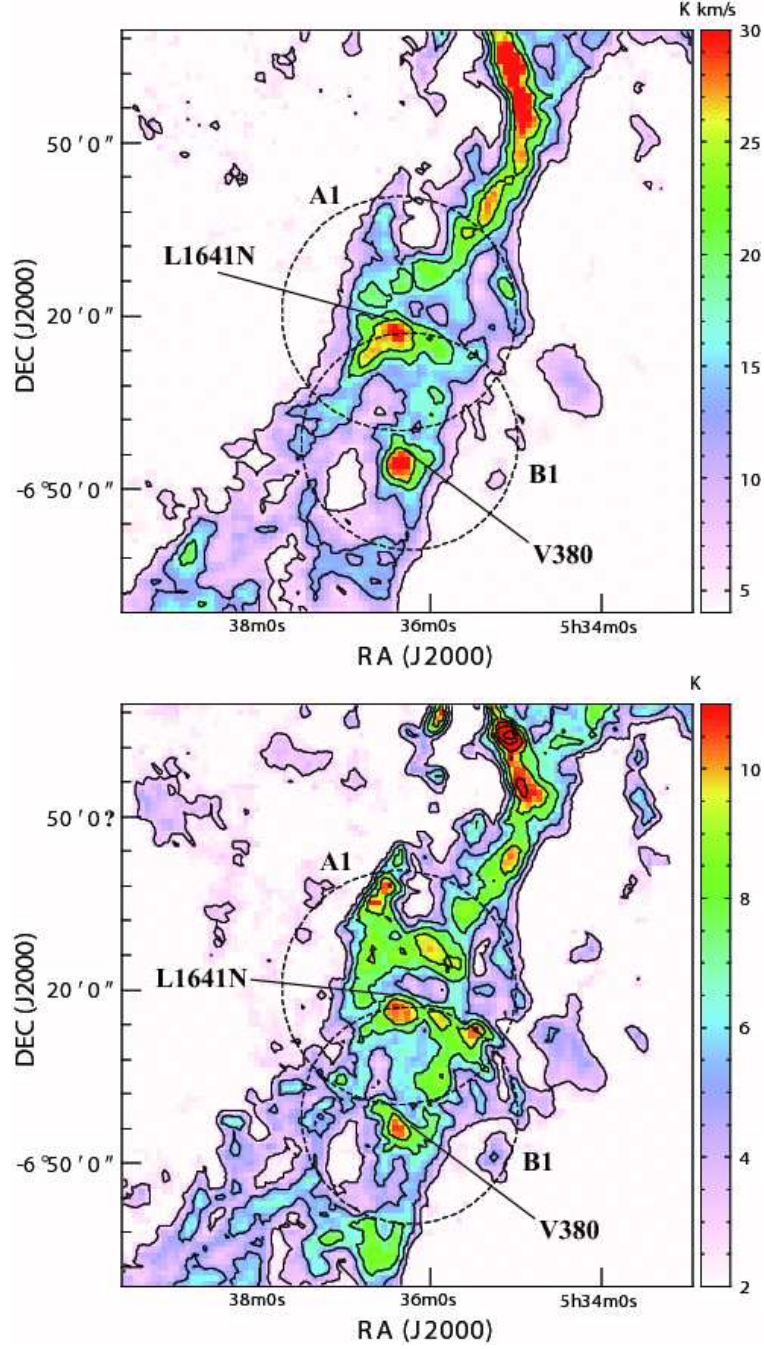


Fig. 12.— (a) ^{13}CO total integrated intensity map in the range from $V_{\text{LSR}} = 1 \text{ km s}^{-1}$ to 14 km s^{-1} (Bally & Langer 1987). (b) ^{13}CO peak intensity map in the same area presented in panel (a). For both the panels, the positions of the circles A1 and B1 presented in Figure 9 are indicated with the dashed lines.